

Dual-layer collimator for improved spatial resolution in SPECT with CZT cameras: An analytical and Monte Carlo study

This paper was downloaded from TechRxiv (<https://www.techrxiv.org>).

LICENSE

CC BY 4.0

SUBMISSION DATE / POSTED DATE

15-10-2021 / 18-10-2021

CITATION

walrand, stephan; Boutaghane, Nasreddine; Hesse, Michel; Bouzid, Boualem; Hospital, Habib Zaidi - Geneva University; Jamar, François (2021): Dual-layer collimator for improved spatial resolution in SPECT with CZT cameras: An analytical and Monte Carlo study. TechRxiv. Preprint.
<https://doi.org/10.36227/techrxiv.16817368.v1>

DOI

[10.36227/techrxiv.16817368.v1](https://doi.org/10.36227/techrxiv.16817368.v1)

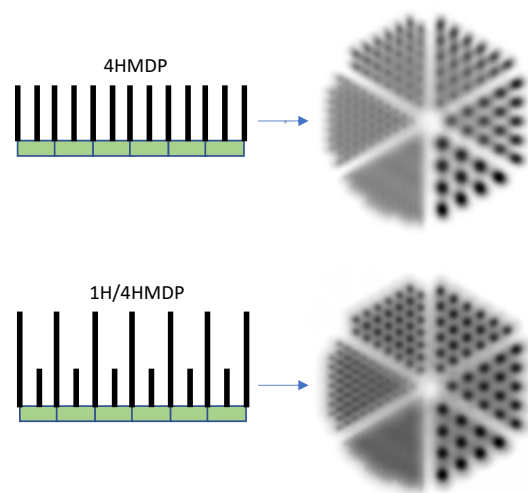
Dual-layer collimator for improved spatial resolution in SPECT with CZT cameras: An analytical and Monte Carlo study

Nasreddine Boutaghane, Michel Hesse, Boualem Bouzid, Habib Zaidi *Fellow, IEEE*,
François Jamar, Stephan Walrand *Member, IEEE*

Abstract— Current hole matching pixel detector (HMPD) collimators for SPECT imaging exist in two configurations: one hole per pixel (1HMPD) or four holes per pixel (4HMPD). The aim of this study was to assess the performance of a dual-layer collimator made by stacking up these two collimator types (1H/4HMDP) for low and medium-energy gamma emitters. Analytical equations describing 1H/4HMDP collimator geometrical efficiency and full width at half maximum (FWHM) were derived. In addition, a fast dedicated gamma ray-tracing Monte Carlo (MC) code was developed to assess the collimator's point spread function (PSF) and to simulate planar and SPECT acquisitions. A relative agreement between analytical equations and MC simulations better than 3% was observed for the efficiency and better than 1% for the FWHM. The length of the two layers was optimized to get the best spatial resolution while keeping the geometrical efficiency equal to that of the 45mm-length 1HMPD collimator. An optimized combination of the 1H/4HMDP configuration with respective hole lengths of 20mm and 12.95mm has been derived. For source-collimator distances above 5 cm and equal collimator geometrical efficiency, the spatial resolution of this optimal 1H/4HMDP collimator supersedes that of the 45mm-length 1HMPD collimator, and that of the 19.1mm-length 4HMPD collimator. This improvement was observed in simulations of bar phantoms planar images and of hot rods phantom SPECT. Remarkably, the spatial resolution was preserved along the depth of the Jaszczak phantom slices. The 1H/4HMDP collimator is a promising solution for CZT SPECT imaging of low- and medium-energy emitters.

Index Terms— SPECT, pixelated detectors, CZT, hole matching pixel detector, Monte Carlo.

Graphical abstract—



Left: schematic representation of the one and dual-layer collimator providing equal efficiency. Right: FBP reconstruction of a high statistics SPECT acquisition of a hot rods insert simulated by Monte Carlo techniques.

I. INTRODUCTION

Since the introduction of the first imaging SPECT camera invented by Anger [1], different design trends have been developed using continuous and pixelated scintillation crystals [2, 3]. A number of constructors have focused on the design of SPECT cameras by optimizing collimators dedicated for the explored organs and for the energies of the used radionuclides. Therefore, to span all the possible radionuclides to image most

Submitted 2021 October 15

N Boutaghane is with University of Sciences and Technology Houari Boumediene, Algiers, Algeria and with Université des Frères Mentouri, Constantine, Algeria, nboutaghane83@yahoo.fr, M Hesse is with Cliniques Universitaires Saint-Luc, Brussels, Belgium michel.hesse@uclouvain.be, B Bouzid is with University of Sciences and Technology Houari Boumediene, Algiers, Algeria, boualem.bouzid@gmail.com, H Zaidi is with Geneva University Hospital, Geneva, Switzerland, habib.zaidi@hcuge.ch, F Jamar is with Cliniques Universitaires Saint-Luc, Brussels, Belgium, francois.jamar@uclouvain.be, S Walrand is with Cliniques Universitaires Saint-Luc, Brussels, Belgium, stephan.walrand@uclouvain.be

Corresponding author: nboutaghane83@yahoo.fr

organs, the exchange of collimators was as adopted along with the parallel-hole collimator, which was proposed since the first images acquire with Anger camera. Before designing this important component, analytical calculations and Monte Carlo modeling have been considered as an important tool to their optimization. Many analytical formulations have been developed for parallel-hole, converging and pinhole collimators [4-7]. Other expressions have also been derived for combining two collimator types [8, 9]. The combination of two parallel-hole collimator types with hexagonal patterns for conventional SPECT imaging has also been proposed [10]. However, this combination was not used with pixelated detectors.

In the last two decades, the developments focused on the replacement of standard detectors-based scintillation crystals by new generations of solid-state pixelated detectors [11]. Various designs involving the development of novel collimators, especially for cardiac imaging, have been explored with these new detectors becoming inevitable to acquire exams with high-quality performance [12, 13]. Nine semi-stationary vertical columns equipped with a one hole matching pixel detector (IHMPD) configuration has been developed by Spectrum Dynamics for the DSPECT system [14]. Gambhir et al. [15] reported that the DSPECT system was ten times faster than the conventional dual-head camera for the same image quality. GE Healthcare has designed the Discovery NM 530c system, which consists of 19 stationary small pixelated CZT detectors focused with 19 pinhole collimators [3, 16]. Kennedy et al. [17] observed that both sensitivity and spatial resolution improved with almost five-fold increase in sensitivity compared to a parallel-hole collimator for myocardial perfusion imaging. Other investigators attempted to use an existing dedicated cardiac DSPECT camera to investigate potential applications in brain [18], thyroid, and parathyroid imaging [19]. However, the special geometry design of these cameras and their unique scanning pattern has limited their applications in body SPECT imaging.

The utility of dedicated pixelated detectors has motivated constructors to focus on general-purpose clinical SPECT imaging. The development of the large pixelated CZT cameras for general-purpose studies appears a sensitive approach and is becoming a mature field. This conceptual design will likely replace traditional large scintillation crystals-based design. To this end, the potential use of a large field-of-view of pixelated CZT detector has recently been introduced by GE Healthcare through the design of the large field-of-view GE NM/CT 870 CZT camera for general-purpose clinical SPECT imaging with different parameter characteristics of the 1HMPD collimators [20]. Spectrum Dynamics introduced a new version of 360-degree CZT VERITON-CT system, also with the 4HMPD configuration [21]. Recently, the full-ring enclosed system (GE StarGuide) has also been developed with the 4HMPD configuration [22].

Until now, the proposed collimators have been designed to advance new clinical SPECT imagers to favor high sensitivity or improved spatial resolution performance. For high sensitivity applications, Weng et al. [23] proposed to use a large pixel

detector matched collimator hole. However, this concept resulted in spatial resolution deterioration. For high-resolution applications, our previous study [24] has also shown that the use of the 4HMPD configuration provides great potential to improve spatial resolution and contrast even when using a low activity. However, the use of this concept with medium energy emitters suffers from an increase in septal penetration fraction. We hypothesize that combining a dual-layer of different parallel-hole collimator characteristics might be a solution to this problem.

The aim of this work was to assess intrinsic dual-layer collimators performance for low and medium energy emitters. To this end, analytical equations describing the geometrical efficiency and the collimators' spatial resolution were derived. In addition, a fast γ -ray tracing Monte Carlo (MC) code was developed to assess the collimator's point spread function (PSF) shape and to simulate planar and SPECT acquisitions.

II. MATERIALS AND METHODS

A. Analytical geometric efficiency

Figure 1 shows a schematic representation of collimator hole cross-section in the x-axis direction. The septa penetration can be taken into account by assuming that the γ -rays can cross the septa within a distance $1/\mu$ to the septa edge (dashed horizontal blue lines) where μ is the attenuation of the septa material.

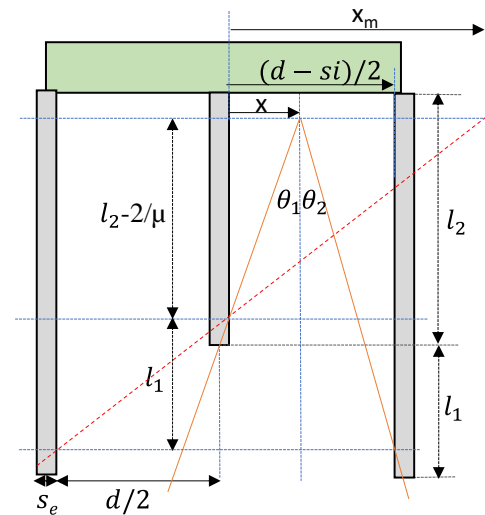


Figure 1: Schematic representation of the two-layer collimator matching one pixel detector (light green). Horizontal blue lines show the extremal limits of the septal γ -rays penetration.

Let's consider the right sub-hole, by choosing the x-axis origin at the inner side of the internal septa of thickness s_i , the intersection x_m of the red line crossing the two left penetration points on the effective top edge of the septa is given by:

$$x_m = (d + s_i) \frac{\tilde{l}_2}{2l_1} \quad (1)$$

where the \sim operator is defined as:

$$\tilde{l} = 1 - 2/\mu \quad \text{if } l > 2/\mu \quad = 0 \text{ otherwise} \quad (2)$$

when $x_m > (d - s_i)/2$ all the γ -rays coming from the left have to cross the internal septa to be detected. This condition can be re-written as:

$$\tilde{l}_2 \geq l_1 \frac{1-s_i/d}{1+s_i/d} \quad (3)$$

$$\text{1st case:} \quad \tilde{l}_2 \geq l_1 \frac{1-s_i/d}{1+s_i/d}$$

Assuming $d/2 \ll l_2$ we get:

$$\theta_1 \approx \frac{x}{l_2} \quad (4)$$

$$\theta_2 \approx \frac{(d-s_i)/2 - x}{l_1+l_2} \quad (5)$$

The effective full angular aperture of the right sub-hole is given by the integral:

$$\theta = \int_0^{(d-s_i)/2} \left(\frac{x}{l_2} + \frac{(d-s_i)/2 - x}{l_1+l_2} \right) dx \quad (6)$$

which trivially gives:

$$\theta = \frac{((d-s_i)/2)^2}{2} \left(\frac{1}{l_1+l_2} + \frac{1}{l_2} \right) \quad (7)$$

for a circular hole, the efficiency according to the spherical coordinates is given by:

$$\frac{1}{4\pi} \int_0^{2\pi} d\phi \int_0^{\theta/2} \sin\theta d\theta = \frac{1}{2} \left(1 - \cos \frac{\theta}{2} \right) \approx \frac{\theta^2}{16} \quad (8)$$

For a square aperture eq. 8 has to be multiplied by the square to inner circle area ratio, i.e. $4/\pi$, taking into account the sub-hole surface density $1/((d + s_e)/2)^2$, we have for the collimator efficiency:

$$g = \frac{4}{\pi} \frac{1}{((d+s_e)/2)^2} \frac{\theta^2}{16} \quad (9)$$

resulting in the final expression:

$$g = \frac{1}{4\pi} \frac{1}{((d+s_e)/2)^2} \left(\frac{((d-s_i)/2)^2}{2} \left(\frac{1}{l_1+l_2} + \frac{1}{l_2} \right) \right)^2 \quad (10)$$

when $l_1 = 0$, eq. 10 reduces to:

$$g = \frac{1}{4\pi} \frac{1}{((d+s_e)/2)^2} \left(\frac{((d-s_i)/2)^2}{\tilde{l}_2} \right)^2 \quad (11)$$

which is the conventional geometric efficiency for a square hole collimator of hole inner size $(d - s_i)/2$ [25].

$$\text{2nd case:} \quad \tilde{l}_2 \leq l_1 \frac{1-s_i/d}{1+s_i/d}$$

Figure 2 shows that in this case the region $x < x_m$ corresponds to γ -rays never intersected by the left septa, while the region $x > x_m$ corresponds to γ -rays never intersected by the internal septa.

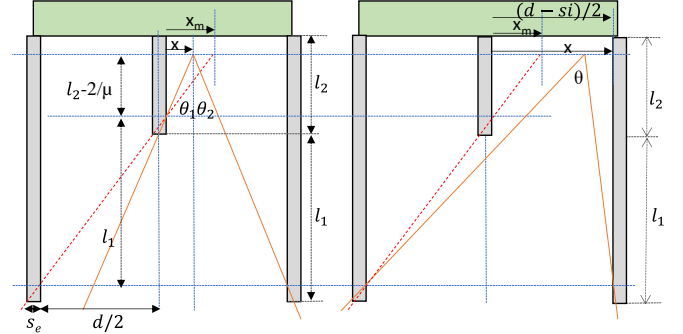


Figure 2: Schematic representation of the two-layer collimator matching one pixel detector (light green). Horizontal blue lines show the extremal limits of the septal γ -rays penetration.

The acceptance angles are given by:

$$\theta_1 \approx \frac{x}{l_2} \quad (12)$$

$$\theta_2 \approx \frac{(d-s_i)/2 - x}{l_1+l_2} \quad (13)$$

$$\theta \approx \frac{d}{l_1+l_2} \quad (14)$$

we have:

$$\theta_1 + \theta_2 \approx \frac{1}{(l_1+l_2)} \left(x \frac{l_1}{l_2} + (d - s_i)/2 \right) \quad (15)$$

The effective total angular aperture of the right sub-hole is given by the integral:

$$\theta = \frac{1}{(l_1+l_2)} \left(\int_0^{(d+s_i)/2} \left(x \frac{l_1}{l_2} + (d - s_i)/2 \right) dx + \int_{(d+s_i)/2}^{l_2} d dx \right) \quad (16)$$

The trivial integration gives:

$$\theta = \frac{1}{2(l_1+l_2)} \left(\frac{(d+s_i)^2}{4} \frac{l_2}{l_1} + \frac{d^2 - s_i^2}{2} \frac{l_2}{l_1} + d(d - s_i - (d + s_i) \frac{l_2}{l_1}) \right) \quad (17)$$

Using eq. 9 we get for the collimator efficiency:

$$g = \frac{1}{4\pi} \frac{1}{(d+s_e)^2} \frac{1}{(l_1+l_2)^2} \left(\frac{(d+s_i)^2}{4} \frac{l_2}{l_1} + \frac{d^2 - s_i^2}{2} \frac{l_2}{l_1} - d(d + s_i) \frac{l_2}{l_1} + d(d - s_i) \right)^2 \quad (18)$$

When $l_2 = 0$ and $s_i = 0$ eq. 18 reduces to:

$$g = \frac{1}{4\pi} \frac{d^2}{(d+s_e)^2} \frac{d^2}{(\tilde{l}_1)^2} \quad (19)$$

which is the conventional square hole collimator efficiency [25].

B. Analytical spatial resolution

The NEMA NU2-2018 protocol for pixelated detector [26] was used for the spatial resolution computation. Analytically this spatial resolution is twice the source shift needed to reduce by twofold the intensity in the pixel detector on which the source was initially centered [27]. Figure 3 shows the two acceptance angles θ_i for a point source shifted by the distance x from the detector pixel center, note that in this computation it is no longer needed to differentiate the two cases.

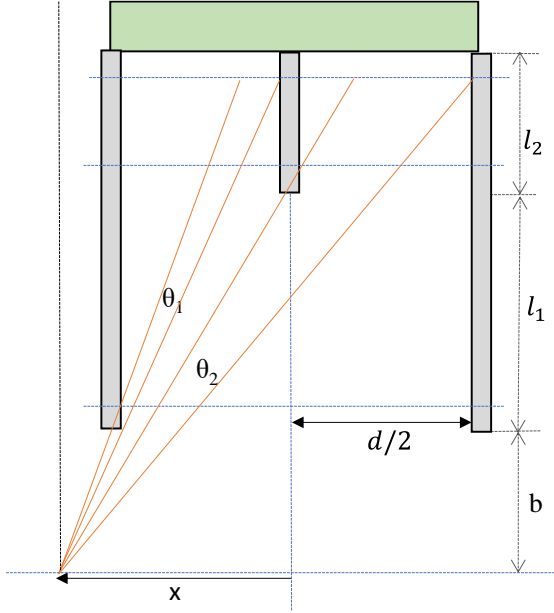


Figure 3: Schematic representation of the two-layer collimator matching one pixel detector (light green). Horizontal blue lines show the extremal limits of the septal γ -rays penetration

The two acceptance angles can be written as the differences of the angles versus the left dashed black line, i.e.:

$$\theta_1(x) \approx \frac{x-s_i/2}{b+l_1+l_2-1/\mu} - \frac{x-d/2}{b+1/\mu} \quad (20)$$

$$\theta_2(x) \approx \frac{x+d/2}{b+l_1+l_2-1/\mu} - \frac{x+s_i/2}{b+1/\mu} \quad (21)$$

the FWHM is given by:

$$\theta_1\left(\frac{\text{FWHM}}{2}\right) + \theta_2\left(\frac{\text{FWHM}}{2}\right) = \frac{1}{2} \frac{d-s_i}{b+l_1+l_2-1/\mu} \quad (22)$$

the left term of eq. 22 being the acceptance when the source is centered in front the hole.

A trivial calculation gives:

$$\text{FWHM} = \left(\frac{d}{b+1/\mu} - \frac{s_i}{b+l_1+1/\mu}\right) / \left(\frac{1}{b+1/\mu} + \frac{1}{b+l_1+1/\mu} - \frac{2}{b+l_1+l_2-1/\mu}\right) \quad (23)$$

C. Monte Carlo code

A fast γ -ray tracing Monte Carlo code modelling the dual-layer collimator coupled to an ideal pixelated detector was developed in visual c++. SIMD oriented fast Mersenne twister random generators were used for uniform random drawing [28]. Scattering was neglected, and the probability of a γ -ray to cross any septa was given by $e^{-\mu l}$ where μ is the septa material attenuation coefficient and l the crossing length within the septa.

For validation, the collimator PSF was also computed using GATE 8.2 [29] for an ideal pixelated detector [26].

D. Dual-layer optimization

The collimator reference was the WEHR lead collimator equipping the GE NM/CT 870 CZT camera, i.e. $\mu = 2.7$ and 0.71 mm^{-1} for 140 and 245 keV γ -rays, respectively. Other parameters were: detector pixel pitch = 2.46 mm, septal thickness $s_e = 0.2$ mm, collimator thickness $l_1 = 45$ mm ($l_2 = 0$), resulting in $g = 1.71\text{E-}4$ using eq. 19.

The layer thickness l_2 was computed as a function of the decreasing l_1 thickness in order to keep the geometric efficiency computed by MC equal to that of the WEHR collimator. Afterwards the geometric efficiency was computed using eq. 10 or 18, and the FWHM of the PSF was assessed with the MC code according to the NEMA 2018 protocol and also computed using eq. 23. Additionally, the spatial resolution was also assessed as the minimal distance between 2 point-sources to distinguish a valley between the 2 point-sources in the intensity profile simulated using the MC code according to the NEMA 2018 protocol.

E. Imaging evaluation

A high statistics bar phantom acquisition in whole-body mode was simulated with the MC code for a distance of 10 cm to the collimator. Whole-body mode acquisition was chosen because it corresponds to the NEMA 2018 protocol PSF assessment for pixelated detector. Also, the spatial resolution for pixelated detector is not uniform in static planar acquisition and locally depends on the transverse distance between activity transition and detector pixel edge position. For bar phantoms this results in moire effect [30].

A high statistics SPECT acquisition of the Ultra deluxe Jaszczak hot rods insert was also simulated with the MC code, the inner diameter of the rods being 3.2, 4.8, 6.4, 7.9, 9.5 and 11.1 mm. The rotation radius was 20 cm, giving rods distances to the collimator ranging from 10 to 19 cm. This distance range is typically met in clinical SPECT imaging. The aim being to evaluate the intrinsic collimators performances, no attenuation and no scattering was applied within the phantom, and the acquisitions were reconstructed with the FBP algorithm of the MIM software 7.1.3 (Cleveland, OH) in a 256x256 matrix (pixel size = 1.23 mm) from 256 simulated angle positions.

III. RESULTS

Table 1 shows the comparison between the analytical equation and the MC simulation for the collimator efficiencies and FWHM. The equations provided a systematic relative overestimation of 2.9 ± 0.8 % for the efficiency. This arise from the fact that the effective length approximation used in the equation derivation neglects that, when the rays become very slanted, it becomes to be intersected by the successive septa. When the septa attenuation increases, the agreement improves (data not shown). On contrary, the FWHM agreement was better than 1%, as the half peak value is reached when the ray still only intersects the hole septum.

l_1 - l_2 [mm](MC)	45-0.00	25-10.75	20-12.95	0-19.20
$g \times 10^4$ (eq. 10 or 18)	1.75	1.78	1.77	1.74
FWHM (MC) [mm]	7.34	6.59	6.52	6.67
FWHM(eq.23) [mm]	7.37	6.63	6.55	6.67

Table 1: Analytical and MC comparison of geometric efficiencies g and FWHM for dual-layer collimator, the layers thickness of which being chosen to get $g = 1.71E-4$ in MC simulations. (see supplementary file for a detailed table with more intermediate 11-12 couples).

The color scaled table 2 shows the FWHM of the dual-layer collimator PSF as a function of the distance to the collimator computed with Monte Carlo according to the NEMA 2018 protocol for pixelated detector. The 20-12.95 collimator was chosen as optimal configuration.

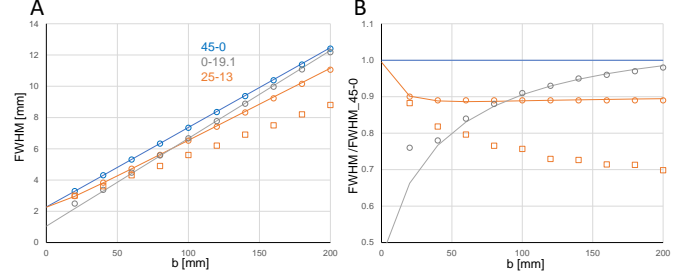
b	45-0.0	40-1.2	35-4.8	30-7.9	25-10.7	20-13.0	15-14.2	10-15.3	5-17.0	0-19.1
2	3.29	3.35	3.19	3.13	3.05	2.97	2.91	2.82	2.61	2.49
4	4.3	4.32	4.12	4.02	3.92	3.83	3.82	3.79	3.64	3.37
6	5.31	5.3	5.06	4.92	4.8	4.72	4.76	4.8	4.7	4.47
8	6.33	6.28	5.99	5.83	5.68	5.61	5.7	5.82	5.76	5.57
10	7.34	7.26	6.93	6.75	6.59	6.52	6.66	6.84	6.84	6.67
12	8.35	8.24	7.87	7.66	7.48	7.41	7.62	7.86	7.91	7.77
14	9.37	9.24	8.81	8.57	8.38	8.32	8.57	8.9	8.97	8.88
16	10.4	10.2	9.74	9.49	9.28	9.23	9.53	9.92	10.1	9.97
18	11.4	11.2	10.7	10.4	10.2	10.2	10.5	11.0	11.1	11.1
20	12.4	12.2	11.6	11.3	11.1	11.1	11.5	12.0	12.2	12.2

Table 2: Color scaled FWHM of the different combined collimators PSF as a function of the distance to the collimator computed with MC according the NEMA 2018 protocol for pixelated.

Fig. 4 shows the collimators FWHM (circles) and spatial resolution (rectangles) as a function of the source-collimator distance b for the three collimators configurations types (1HMPD, optimal 1H/4HMPD and 4HMPD) for 140 keV γ -rays. Spatial resolution was found equal to the FWHM for the mono-layer 1HMPD and 4HMPD collimators, but not for dual-layer 1H/4HMPD collimators.

Figure 4: A: FWHM and spatial resolution at 140 keV as a function of the distance b to the collimator as defined by the NEMA 2018

protocol for pixelated detector. blue: 1HMPD 45mm, orange: optimal



combined, gray: 4HMPD. Lines: eq. 23. Circles: FWHM computed with MC. Squares: spatial resolution computed with MC. B: ratio to the 1HMPD 45mm.

Fig. 5A,5C show the intensity profile at 140 and 245 keV for a point source at 10 cm computed by MC according to NEMA 2018 protocol for pixelated detector. All collimators exhibit constant long tails at 245 keV, especially the 4HMPD collimator the tails of which being twice that of the two other ones. The optimal dual-layer collimator PSF exhibits a narrow shoulder below 30% of the peak value. We will come back on this apparent drawback in the discussion section.

Fig. 5B shows the intensity profile at 140 keV for 2 point-sources at 10 cm and separated by the collimator FWHM+0.1mm, i.e. 7.34, 6.52 and 6.67 mm (see table 2). Note that the valley between the two source peaks is much deeper for the optimal 1H/4HMPD collimator. In fact, the optimal collimator gives the same valley deepness than the two other ones for a shift of only 5.5 mm which can be considered as the actual spatial resolution of this collimator.

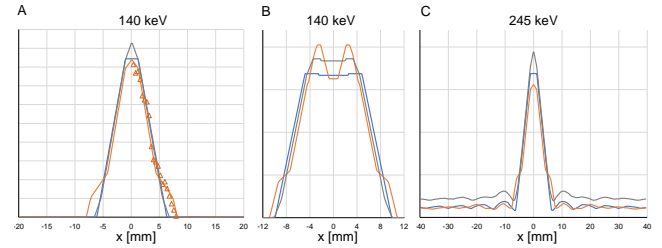


Figure 5: A,C: Intensity profile (arbitrary unit) at 140 ($\mu=2.73\text{mm}^{-1}$) and 245 keV ($\mu=0.71\text{mm}^{-1}$) for one point source at 10 cm computed by MC according to the NEMA 2018 protocol for pixelated detector. blue: 45mm 1HMPD, orange: 1H/4HMPD, gray: 4HMPD. Triangles: GATE simulation. Note the long constant tails at 245 keV. B: Intensity profile of two point-sources at 10 cm separated by the collimator FWHM+0.1mm.

Fig. 6 shows the MC simulation of whole-body mode acquisitions of bar phantoms located 10 cm far away from the collimator.

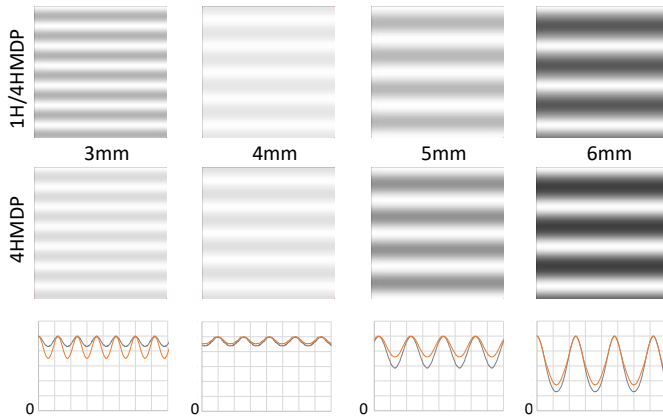


Figure 6: High statistics MC simulation of bar phantoms acquired in whole-body mode. Orange and grey curves: 1H/4HMDP and 4HMDP vertical profiles, respectively. Note the better contrast and valley deepness obtained by the 1H/4HMDP collimator for the 3 mm bar phantom.

Fig. 7 shows FBP reconstructed slices of the high statistics SPECT acquisition of the Ultra deluxe Jaszczak hot rods insert simulated by the MC code

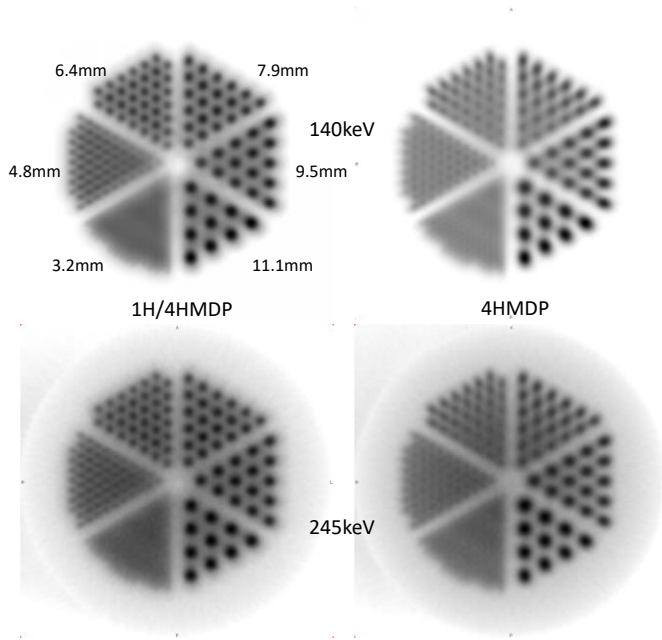


Figure 7: FBP reconstructed slice of the high statistics SPECT acquisition of the Ultra deluxe Jaszczak hot rods insert simulated with the MC code for a rotation radius of 20 cm. Left and right column: using the 1H/4HMDP and 4HMDP collimators, respectively. Upper and lower rows: MC simulations for 140 and 245 keV primary γ -rays, respectively. Note the much better contrast preservation versus the deepness for the 1H/4HMDP collimator and the right circular shape of the outer rods.

IV. DISCUSSION

The study showed a relative agreement between the analytical equations and the MC simulations better than 3 and 1 % for the

efficiency and the FWHM, respectively (table 1). This agreement is a mutual cross-validation of the MC code and of the analytical equations. Furthermore, in the limit of the single layer collimator, these equations rightly reduce to the conventional efficiency and FWHM ones. Last, GATE simulation validated the 1H/4HMDP collimator PSF obtained with our fast MC code.

The results showed that for an equal efficiency, the optimal 1H/4HMDP collimator provided: 1) a better spatial resolution than the 1HMDP one (Fig. 4); 2) a better spatial resolution than the 4HMDP one for distances above 5 cm that are typically met in clinical SPECT imaging (Fig. 4); 3) long constant tails at 245 keV twice lower than those observed with the 4HMDP collimator (Fig. 5C); 4) a deeper profile valley for two sources separated by the collimator FWHM (Fig. 5B).

The spatial resolution is the minimal distance between 2 point-sources needed to distinguish 2 peaks in the intensity profile crossing the 2 sources. The spatial resolution is commonly assimilated to the FWHM of the PSF. In fact, this equality is only exact for triangular PSF which gives a constant intensity profile between 2 point-sources separated by the FWHM. However, this approximation is quite accurate for gaussian shaped PSF.

The 1H/4HMDP PSF exhibits a shoulder on the low region confirmed by the GATE simulation (Fig. 5A). When the distance between two sources is smaller than the FWHM, the shoulder of one source is added to the peak position of the other one, and reciprocally. As a result, the valley deepness is increased (Fig. 5B). For this, it is mandatory for best spatial resolution evaluation to use another alternative of the isolated punctual source as well as the bar and Jaszczak phantoms. Fig. 6-7 show that this feature improves the visualization of pattern scale lower than the FWHM, but at the cost of a little bit lower contrast for pattern scale larger than the FWHM. Remarkably, Fig. 7 shows that the contrast using the 1H/4HMDP is well preserved when moving away from the collimator. This better spatial resolution uniformity results in a better reproduction of the circular shape of the outer rods. These two benefits hold for 245 keV γ -rays.

This amazing benefit of having a shoulder in the PSF is a paradigm shift. Indeed, it is commonly accepted that faster is the PSF decrease, better is the spatial resolution. In contrary, the present simulations show that a narrow shoulder can improve the spatial resolution. Despite an extensive literature search among collimator or optical lenses studies, we did not find any other works describing this effect. Theoretical and simulation studies to determine the optimal shoulder shape will be valuable. However, the design and building of the collimator enabling the optimal PSF shape could be highly challenging and even impossible.

Our study has the limitation of neglecting the intra-septa scattering. This choice was justified by the intent to cross validate the MC code with analytical equations in which septa scattering cannot be modeled. Another reason was to obtain a fast MC code allowing fast SPECT simulation in order to make easier a first optimization of the collimator parameters. Last, the

GATE simulation of the PSF which included intra-septa scattering is very similar to that obtained with the fast MC code.

Obviously, real CZT-1H/4HMDP performance will be hampered by statistical noise and intra phantom or patient attenuation and scattering. However, this preliminary study was to evaluate the intrinsic collimator performances. These intrinsic performances will still have to be evaluate in non-conventional SPECT samplings such as performed in the GE StarGuide and in the Spectrum-Dynamics VERITON-CT system [22]. Further realistic SPECT acquisition using full-physics MC code will have to be performed

V. CONCLUSION

For source-collimator distance above 5 cm and equal geometrical collimator efficiency, the spatial resolution of the optimal 1H/4HMDP collimator supersedes that of the 45mm-length 1HMPD collimator, as well as that of the 19.1mm-length 4HMPD collimator (Fig.4B). This improvement was observed in simulated bar phantoms planar imaging and in hot rods phantom SPECT. Remarkably, the spatial resolution was preserved on the whole deepness of the Jaszczak phantom. The newly proposed combined collimator was investigated to be another solution to the existing parallel-hole collimators for large field-of-view of pixelated CZT detector and full-ring enclosed detector for low and medium energy emitters

REFERENCES

- [1] H. O. Anger, "Scintillation Camera," *Review of Scientific Instruments*, vol. 29, no. 1, pp. 27-33, 1958, doi: 10.1063/1.1715998.
- [2] E. Gordon DePuey "Advances in SPECT camera software and hardware: Currently available and new on the horizon," *J Nucl Cardiol*, vol. 16, pp. 551-81, 2012.
- [3] E.V. Garcia, T.L. Faber, and F.P. Esteves, "Cardiac dedicated ultrafast SPECT cameras: new designs and clinical implications," *J Nucl Med*, vol. 52, no. 2, pp. 210-7, Feb 2011, doi: 10.2967/jnumed.110.081323.
- [4] A. R. Formiconi, "Geometrical response of multihole collimators," *Phys. Med. Biol.*, vol. 43 1998.
- [5] L. R. Pato, S. Vandenberghe, T. Zedda, and R. Van Holen, "Parallel-hole collimator concept for stationary SPECT imaging," *Physics in medicine and biology*, vol. 60, no. 22, pp. 8791-807, Nov 21 2015, doi: 10.1088/0031-9155/60/22/8791.
- [6] A. L. Weinmann, C. B. Hruska, and M. K. O'Connor, "Design of optimal collimation for dedicated molecular breast imaging systems," *Medical physics*, vol. 36, no. 3, pp. 845-56, Mar 2009, doi: 10.1118/1.3077119.
- [7] J. van Roosmalen and M. C. Goorden, "Non-diverging analytical expression for the sensitivity of converging SPECT collimators," *Physics in medicine and biology*, vol. 62, no. 10, pp. N228-N243, 2017, doi: 10.1088/1361-6560/aa6646.
- [8] B. M. W. Tsui; and G. T. Gullberg, "The geometric transfer function for cone and fan beam collimators," *Phys. Med. Biol.*, vol. 35, no. 1, p. 13, 1990.
- [9] M. C. Rentmeester, F. van der Have, and F. J. Beekman, "Optimizing multi-pinhole SPECT geometries using an analytical model," *Physics in medicine and biology*, vol. 52, no. 9, pp. 2567-81, May 7 2007, doi: 10.1088/0031-9155/52/9/016.
- [10] Y. Li, P. Xiao, X. Zhu, and Q. Xie, "Multi-resolution multi-sensitivity design for parallel-hole SPECT collimators," *Physics in medicine and biology*, vol. 61, no. 14, pp. 5390-405, Jul 21 2016, doi: 10.1088/0031-9155/61/14/5390.
- [11] M.A. Park, S.C. Moore, S.P. Muller, S.J. McQuaid, and M.F. Kijewski, "Performance of a high-sensitivity dedicated cardiac SPECT scanner for striatal uptake quantification in the brain based on analysis of projection data," *Med Phys*, vol. 40, no. 4, p. 042504, Apr 2013, doi: 10.1118/1.4794488.
- [12] B.F. Hutton, "New SPECT technology: potential and challenges," *Eur J Nucl Med Mol Imaging*, vol. 37, p. 4, 2010.
- [13] G. Germano, P. J. Slomka, and D. S. Berman, "New Hardware Solutions for Cardiac SPECT Imaging," *Current Cardiovascular Imaging Reports*, vol. 6, no. 4, pp. 305-313, 2013, doi: 10.1007/s12410-013-9206-4.
- [14] Erlandsson K, K. Kacperski, D. van Gramberg, and B. F. Hutton, "Performance evaluation of D-SPECT: a novel SPECT system for nuclear cardiology," *Phys Med Biol*, vol. 54, no. 9, pp. 2635-49, May 07 2009, doi: 10.1088/0031-9155/54/9/003.
- [15] S. S. Gambhir *et al.*, "A Novel High-Sensitivity Rapid-Acquisition Single-Photon Cardiac Imaging Camera," *Journal of nuclear medicine : official publication, Society of Nuclear Medicine*, vol. 50, p. 8, 2009, doi: 10.2967/jnumed.108.060020.
- [16] P. J. Slomka, J. A. Patton, D. S. Berman, and G. Germano, "Advances in technical aspects of myocardial perfusion SPECT imaging," *J Nucl Cardiol*, vol. 16, no. 2, pp. 255-76, Mar-Apr 2009, doi: 10.1007/s12350-009-9052-6.
- [17] J.A. Kennedy, O. Israel, and A. Frenkel, "3D iteratively reconstructed spatial resolution map and sensitivity characterization of a dedicated cardiac SPECT camera," *J Nucl Cardiol*, vol. 21, no. 3, pp. 443-52, Jun 2014, doi: 10.1007/s12350-013-9851-7.
- [18] M. A. Park, S. C. Moore, S. P. Muller, S. J. McQuaid, and M. F. Kijewski, "Performance of a high-sensitivity dedicated cardiac SPECT scanner for striatal uptake quantification in the brain based on analysis of projection data," *Medical physics*, vol. 40, no. 4, p. 042504, Apr 2013, doi: 10.1118/1.4794488.

- [19] Y. Miyazaki, Y. Kato, A. Imoto, and K. Fukuchi, "Imaging of the thyroid and parathyroid using a cardiac cadmium zinc telluride camera: Phantom studies," *Journal of nuclear medicine technology*, Nov 10 2017, doi: 10.2967/jnmt.117.199042.
- [20] T. Ito *et al.*, "Experimental evaluation of the GE NM/CT 870 CZT clinical SPECT system equipped with WEHR and MEHRS collimator," *Journal of applied clinical medical physics*, vol. 22, no. 2, pp. 165-177, Feb 2021, doi: 10.1002/acm2.13158.
- [21] C. Desmonts, M. A. Bouthiba, B. Enilorac, C. Nganoa, D. Agostini, and N. Aide, "Evaluation of a new multipurpose whole-body CzT-based camera: comparison with a dual-head Anger camera and first clinical images," *EJNMMI Phys*, vol. 7, no. 1, p. 18, Mar 17 2020, doi: 10.1186/s40658-020-0284-5.
- [22] D. Serre *et al.*, "Apport des caméras CZT grand champ 2D et 3D dans l'évolution des pratiques cliniques," *Médecine Nucléaire*, vol. 45, no. 4, pp. 234-239, 2021, doi: 10.1016/j.mednuc.2021.06.135.
- [23] F. Weng, S. Bagchi, Y. Zan, Q. Huang, and Y. Seo, "An energy-optimized collimator design for a CZT-based SPECT camera," *Nucl Instrum Methods Phys Res A*, vol. 806, pp. 330-339, Jan 11 2016, doi: 10.1016/j.nima.2015.09.115.
- [24] N. Boutaghane, B. Bouzid, and H. Zaidi, "Conceptual design of a large pixelated CZT detector with four-hole collimator matched pixel detector for SPECT imaging: a Monte Carlo simulation study," *Journal of Instrumentation*, vol. 14, no. 02, pp. P02026-P02026, 2019, doi: 10.1088/1748-0221/14/02/p02026.
- [25] S. R. Cherry, J. A. Sorenson, and M. E. Phelps, *Physics in nuclear medicine e-Book*. Elsevier Health Sciences, 2012.
- [26] NEMA. https://www.nema.org/docs/default-source/standards-document-library/nema-nu-2-2018-contents-and-scope.pdf?sfvrsn=1238765f_1 (accessed).
- [27] W. Siman and S. Cheenu Kappadath, "Performance characteristics of a new pixelated portable gamma camera," *Medical physics*, vol. 39, no. 6Part1, pp. 3435-3444, 2012.
- [28] M. Saito; and M. Matsumonto. "SIMD-oriented Fast Mersenne Twister (SFMT): twice faster than Mersenne Twister." <http://www.math.sci.hiroshima-u.ac.jp/~m-mat/MT/SFMT/index.html> (accessed).
- [29] D. Sarrut *et al.*, "A review of the use and potential of the GATE Monte Carlo simulation code for radiation therapy and dosimetry applications," *Medical physics*, vol. 41, no. 6Part1, p. 064301, 2014.
- [30] J. Kim, S.-K. Kim, and V. Saveljev, "Moiré effect in displays: a tutorial," *Optical Engineering*, vol. 57, no. 03, p. 1, 2018, doi: 10.1117/1.oe.57.3.030803.